Wake Vortex Interaction of Urban Air Mobility Aircraft

Nhan Nguyen*
NASA Ames Research Center, Moffett Field, CA 94035
Graeson Bartolini†
NASA Ames Research Center, Moffett Field, CA 94035
Joshua Baculi‡
HX5, LLC., Fort Walton Beach, FL 32548
Wendy A. Okolo§
NASA Ames Research Center, Moffett Field, CA 94035
Juntao Xiong¶
KBR Wyle, Inc., Moffett Field, CA 94035

This paper presents a study of wake vortex interaction modeling for urban air mobility. Wake vortex modeling approaches for fixed-wing aircraft and rotorcraft are investigated. A wake age model is developed that accounts for the temporal and spatial dissipation of the wake-induced downwash. A wake vortex model is developed for rotorcraft that accounts for blade flapping motion and cyclic pitch control to reduce the lift asymmetry. This in turn results in an equal lift circulation strength on the advancing side and retreating side of the rotor. Two wake vortex interaction simulations are performed to illustrate the modeling approaches.

I. Introduction

The current and forecasted increased population density in many urban and regional areas is precipitating the development of technologies that will enable the Urban Air Mobility (UAM) concept to transport people and goods within urban and metropolitan areas. UAM is envisioned to include the flights, operations, vehicles, standards, and infrastructure that will facilitate this transformation of the national airspace to repeatedly accommodate significantly more flights and passengers, with a high level of autonomy. Thus, a paradigm shift is required to enable safe operations in the national airspace (NAS), using an integrated approach to safety that addresses potential risks to UAM vehicle design and operations.

Under NASA's Aeronautics Research Mission Directorate (ARMD) portfolio, the System-Wide Safety (SWS) project is developing and demonstrating innovative safety-oriented solutions for emerging operations such as small Unmanned Aircraft Systems (sUAS) and UAM.[1] Through the SWS project, hazards to emerging operations are identified such as critical system failures, propulsion component degradation, engine/power failure, or vehicle wake vortex interactions leading to potential loss of control.[2] For these hazards, quantifiable safety metrics are defined and models to monitor and predict their evolution can be developed based on data-driven and/or physics-based techniques. A holistic assessment of current and predicted states of these predefined metrics can be done at various time instances to develop an integrated picture of risk to safe UAM operations. These "in-time" assessments of risk can be utilized to alert autonomous or human-in-the loop decision-makers, thus enabling early mitigation of potential safety hazards to UAM operations.

*Senior Research Scientist and Technical Group Lead of Advanced Control and Evolvable Systems Group, Intelligent Systems Division, AIAA Associate Fellow, nhan.t.nguyen@nasa.gov
†NASA Pathway Intern, Intelligent Systems Division, graeson.l.bartolini@nasa.gov
‡Aerospace Engineer, Intelligent Systems Division, joshua.e.baculi@nasa.gov
§Research Scientist, Intelligent Systems Division, wendy.a.okolo@nasa.gov
¶Aerospace Engineer, Intelligent System Division, juntao.xiong@nasa.gov

This paper investigates the building blocks to model, simulate, and develop a safety service for UAM operations based on wake vortex interactions between UAM vehicles. Aircraft vortex development, propagation, and interactions have been studied extensively for conventional, piloted, fixed-wing aircraft operating at high altitudes.[3] These studies have guided standards and minimum separation requirements for traditional aircraft, enabling safety of conventional aircraft operations.[4] However, for emerging UAM operations, wake vortices created by UAM vehicles operating at lower altitudes, including their interactions with each other, buildings and other urban infrastructure, have not been quantified.

Research is being conducted to develop autonomous formation flight and decentralized operations in the vertiport terminal area for UAM under NASA's ARMD Transformational Tools and Technologies (TTT) project. One major factor which presents a tall pole in the research is the separation criterion for UAM vehicles. There is no consensus on what is considered to be an acceptable safe separation distance since there is a plethora of UAM vehicles being proposed and developed. There is no history of operation with the class of proposed UAM vehicles. Safe separation criteria developed for large transport-class aircraft may not be appropriate for UAM since most of these UAM vehicles are envisioned to carry a lot fewer passengers and therefore are much smaller. To make matters worse, these UAM vehicles are supposed to operate in urban environments at low altitudes. Aerodynamic interactions with buildings can create safety issues to these vehicles. Interactions with other vehicles can create equally dangerous situations as these vehicles are generally much more susceptible to wake and gust encounters due to their low gross weights.

To date, research on autonomy of UAM traffic management does not always use physics-based models to develop autonomous capabilities and coordinated control technologies that account for the spatial interactions of the multi-vehicle system among themselves and with the pilots and air traffic controllers. Separation criteria are usually assumed based on the well-established operational history of passenger transport-class aircraft operation. The present study presents an approach to address this need by proposing a spatial wake interactional model for UAM aircraft comprising both fixed-wing aircraft and rotorcraft. The physics-based model could potentially provide information on how to safely manage and to develop autonomous capabilities for this new class of aircraft toward the goal of increasing the throughput of the UAM traffic. Accurately modeling and quantifying UAM wake vortices will enable operators to understand and predict the magnitude and directions of wake vortices in surrounding areas of the airspace occupied by UAM vehicles. This work can also guide the development of standards and regulations for minimum separation distances between UAM vehicles.

In our initial study, a wake interactional modeling approach has been developed for fixed-wing aircraft and rotorcraft.[5] A simulation of three UAM vehicles flying in close proximity has been performed. The simulation results show a substantial loss of controllability of the trailing aircraft due to a partial wing stall as it encounters the wake vortices shed off by the leading aircraft.[5] In this study, we will extend the previous work[5] to improve the wake vortex model for rotorcraft and to investigate the wake age effect that accounts for the temporal dissipation of the wake vortices in the atmosphere. The wake vortex model for rotorcraft in the previous study assumes a rigid rotor and does not account for blade flapping effect or cyclic pitch control as they usually exist in articulated hinged rotors. As a result, dissimilar wake vortices are produced. This study will revise the rotor wake model to allow for the blade flapping motion. The Lamb-Oseen wake age model accounts for the vortex growth and viscous dissipation based on a simple diffusion model which predicts the wake vortex decay over a much longer timescale. In the initial study, the wake vortex decay appears to be a very slow process which seems to be physically unrealistic. In practice, there are many conditions that affect wake vortex decay. Advection by winds is one effect on the wake vortex decay. Turbulence mixing in the atmosphere could also accelerate the wake vortex delay. A more realistic wake vortex decay model is developed in this study based on a study by Proctor et al.[6]

This paper is organized as follows. In Section II, we model the wake vortices of fixed-wing aircraft, the wake age and propagation effects, the lift circulation of rotorcraft with the blade flapping motion and cyclic pitch control, and the wake vortex interaction of aircraft in maneuvering flights. In Section III, we provide two simulations to illustrate the wake vortex interaction modeling approach. We conclude with a brief remark on possible directions for future work.

II. Wake Vortex Interaction Modeling

A UAM system comprises multiple agents which include UAM vehicles, pilots, operators, and air traffic controllers. Each of these agents could have different behaviors, response time, and goals. Some agents are modeled as continuous-time systems such as vehicles while other agents are high-level decision makers who only command high-level goals and objectives to be executed by the pilots interacting with the vehicles.

The system operates over an airspace defined by a three-dimensional volume (x, y, z) as shown in Figure 1. The airspace volume is discretized into a finite set of grid points. The UAM vehicles flying in this airspace will have spatial interactions with other vehicles and adjacent building structures due to the wake formation. The wake formation at a point in this airspace is time-varying due to the multiple wakes shed by the UAM vehicles.

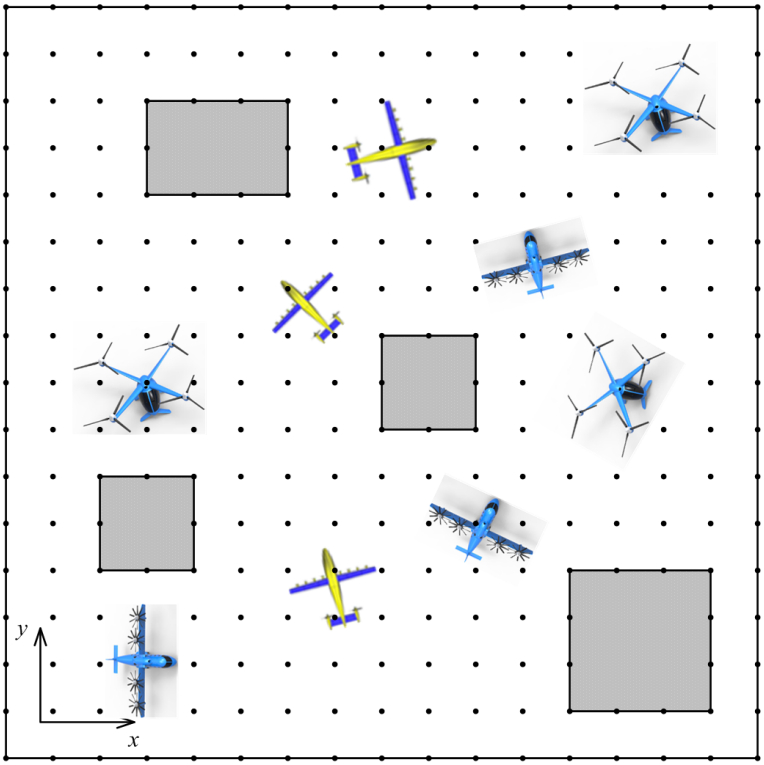

Figure 1. UAM Airspace

Figure 2 illustrates a spatial interaction scenario involving three UAM vehicles operating in close proximity. The two vehicles on the left and the right create two wing tip vortices that interact with each other. These wake vortices generate rolling moments on the two vehicles, thereby potentially causing these vehicles to depart from the intended trajectories. Automatic wing level controls are assumed to be available and are modeled, but these control authorities could be exceeded as the separation becomes too small. The vehicle in the middle feels the wake vortices shed by the two vehicles ahead of it. Depending on the dissipation of this velocity disturbance, this vehicle could experience an increase in the angle of attack and could potentially encounter stall which could lead to safety issues to itself and nearby vehicles.

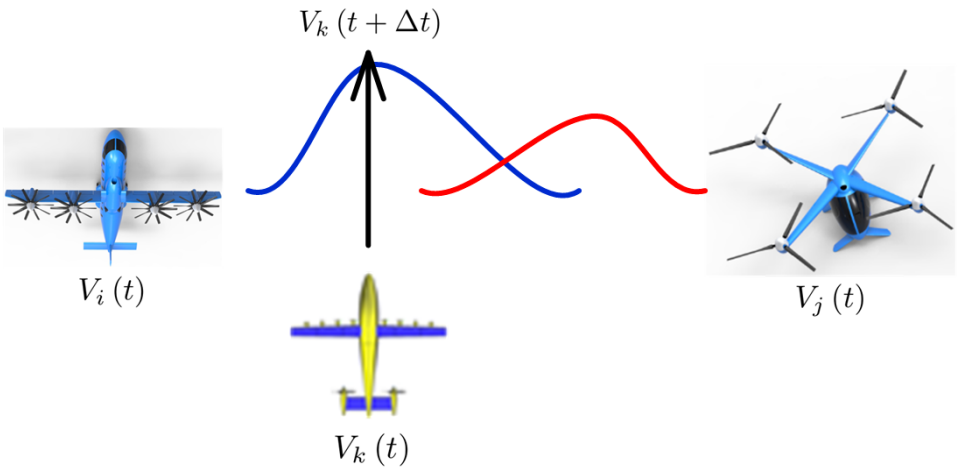

Figure 2. UAM Vehicle Interactions

A. Performance Models of UAM Vehicles

The UAM vehicles will include both types of fixed-wing aircraft and rotorcraft. A simplified performance model of a UAM fixed-wing aircraft can be abstracted as a rectangular lifting surface as shown in Figure 3. Similarly, a UAM rotorcraft can be abstracted as a rotor as shown in Figure 4.

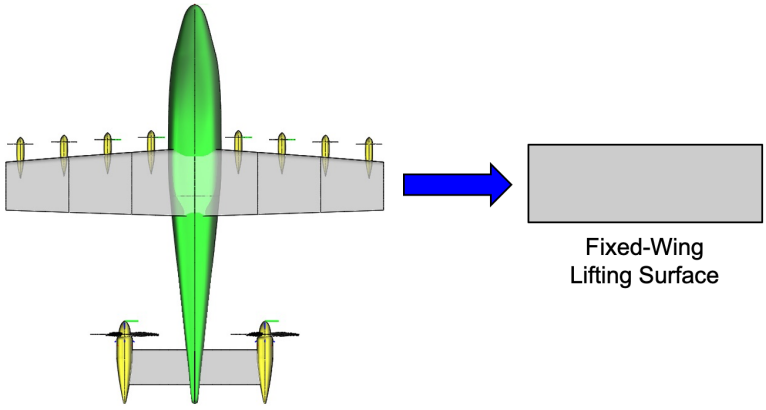

Figure 3. Simplified Performance Model of UAM Fixed-Wing Aircraft

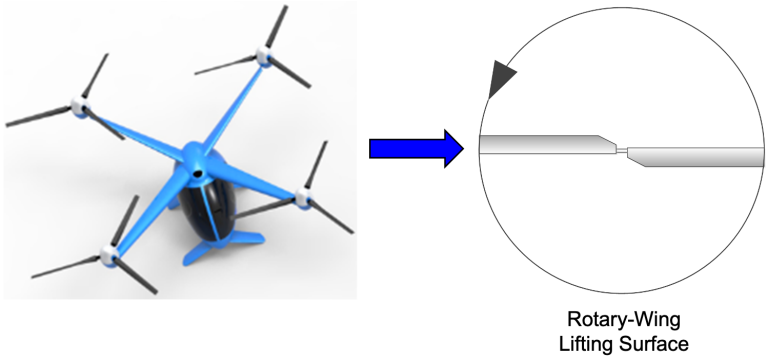

Figure 4. Simplified Performance Model of UAM Rotorcraft

Each UAM vehicle is defined by a set of performance and geometry parameters which include

- Wing span or rotor diameter b for lifting surface
- Lifting surface area S which is assumed to be equal to $b\bar{c}$ for a wing with an average chord $\bar{c}$.
- Aircraft gross weight W
- Rotor speed Ω
- Span efficiency factor ε
- Aircraft maximum thrust T_{max}
- Positive stall angle of attack α_{max}
- Other pertinent parameters

This simplified performance model is agnostic to the detail aircraft configuration. Thus, it does not require a detail aerodynamic model of the UAM vehicle.

B. Wake Vortex Models of Fixed-Wing Aircraft

Wake vortices are shed by all aircraft as a consequence of lift creation. The wake vortices are formed as a consequence of a three-dimensional flow that results in a high pressure distribution on the lower wing surface and a low pressure distribution on the upper wing surface. A spanwise flow thus exists that generates a flow circulation from the lower surface to the upper surface at the wing tip. This flow circulation creates a pair of counter-rotating wake vortices that are shed downstream of the wing as illustrated in Figure 5.

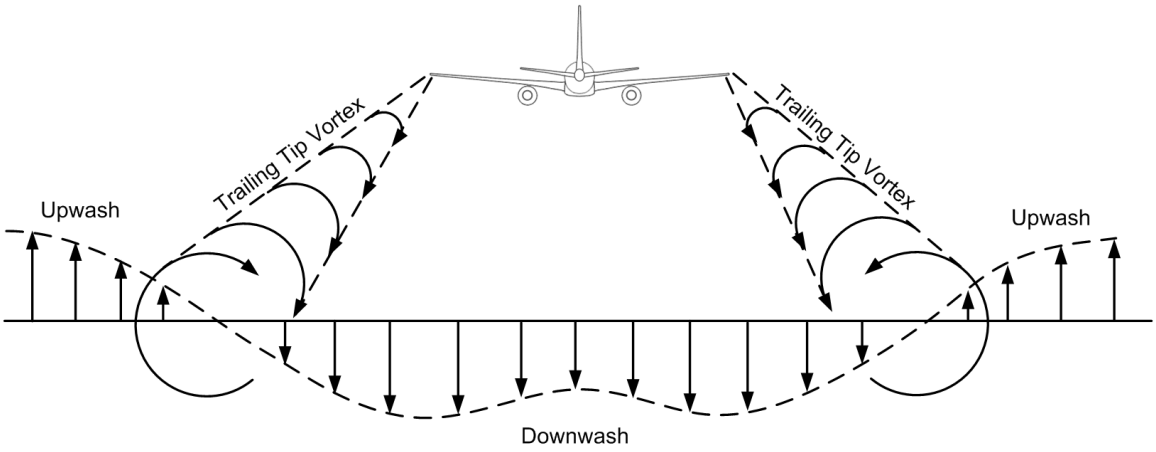

Figure 5. Wake Vortices of Aircraft

The circulation creates a flow field around the wing tips that extends into the fluid well beyond the aircraft. The flow field induced by a wing tip vortex could be understood by a simple potential flow two-dimensional vortex model[7] described by

$$v_\theta = \frac{\Gamma_0}{2\pi r} \tag{1}$$

where v_θ is the wake-induced tangential velocity at a radial position r and Γ_0 is the circulation strength of the vortex. This simple model generally describes the far-field flow at some distance away from the region near the center of the vortex. This region is called a vortex core. The potential wake vortex model breaks down at $r = 0$ where it predicts infinite wake-induced velocity. The flow at the wing tip is three-dimensional and therefore cannot be captured by a simple potential wake vortex model. The lift distribution on an aircraft wing typically goes to zero at the wing tip as illustrated in Fig. 6. This zero lift condition at the wing tip requires that the wake-induced tangential velocity at the center of the wing tip be zero.

The Lamb-Oseen wake vortex model is frequently used in wake vortex modeling to describe the behavior of a wake vortex shed by an aircraft in the vortex core region as well as in the far-field region. The model is described by[8]

$$v_\theta = \frac{\Gamma_0}{2\pi r}\left[1 - e^{-\alpha_L\left(\frac{r}{r_c}\right)^2}\right] \tag{2}$$

where r_c is the vortex core radius and $\alpha_L = 1.25643$. This model prescribes a zero tangential velocity at $r = 0$ and asymptotically tends to the potential wake vortex model as $r \to \infty$.

The Lamb-Oseen model also describes the growth of the wake vortex core with time[9,10] by

$$r_c(t) = \sqrt{4\alpha_L \nu t} \tag{3}$$

where $r_c(t)$ is the wake vortex core starting from a zero core radius at $t = 0$ and ν is the kinematic viscosity coefficient. The wake vortex growth is due to the viscous dissipation in the atmosphere which accounts for the effect of wake vortex aging. The Lamb-Oseen wake vortex growth model starts with a zero core radius at $t = 0$. If the initial core radius r_c is given at $t = 0$, then the model is adjusted to account for the starting wake vortex core at r_c as

$$r_c(t) = \sqrt{r_c^2(0) + 4\alpha_L \nu t} \tag{4}$$

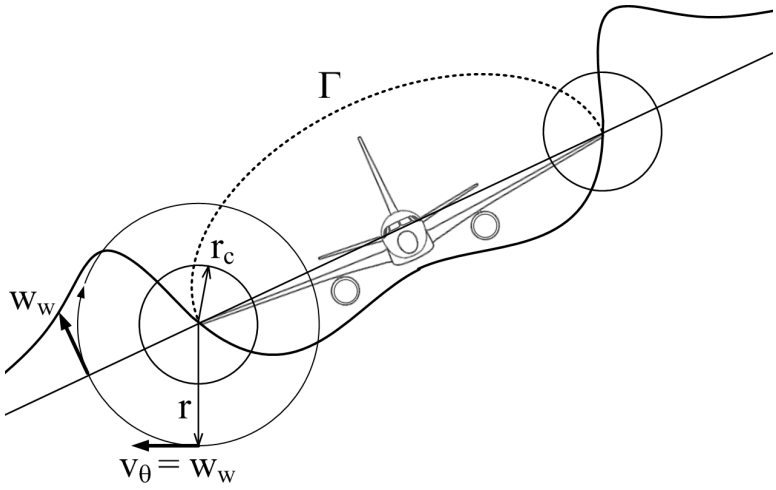

Figure 6. Downwash Distribution

The Lamb-Oseen model is developed through fluid dynamics theory and does not necessarily model wake vortices for aircraft accurately. A wake vortex model has been proposed by Proctor[11] based on flight measurements of fixed-wing aircraft. The model adds an amplitude correction term to the Lamb-Oseen model as shown below:

$$w_w = \begin{cases} \frac{\Gamma_0}{2\pi r}\left[1 - e^{-10\left(\frac{1.4 r_c}{b}\right)^{0.75}}\right]\left[\frac{1 - e^{-\alpha_P\left(\frac{r}{r_c}\right)^2}}{1 - e^{-\alpha_P (1.4)^2}}\right] & r \le 1.4 r_c \\ \frac{\Gamma_0}{2\pi r}\left[1 - e^{-10\left(\frac{|r|}{b}\right)^{0.75}}\right] & r > 1.4 r_c \end{cases} \tag{5}$$

where $\alpha_P = 1.2527$, w_w is the wake-induced normal velocity component or downwash in the aircraft body-fixed reference frame as shown in Figure 6 and b is the wing span. The wake-induced velocity is effectively the tangential velocity component normal to the aircraft plane. So it can be resolved into the three components at a point in the (x, y, z) inertial reference frame where the x-axis points north, y-axis points east, and z-axis points toward the earth's center. The correction term accounts for the effect of the aircraft wing span which is not present in the Lamb-Oseen model. The author should note that Proctor uses r instead $|r|$ in his formula for $r > 1.4 r_c$. If r is interpreted as a wing station measured from the wing tip, r can be negative, hence $|r|$ is used instead.

The Lamb-Oseen and Proctor wake vortex models prescribe a wake-induced downwash distribution at the initial time. The effect of aging of a wake vortex is due to the viscous dissipation. The Lamb model provides the following wake vortex aging effect:[8,12]

$$v_\theta(t) = v_\theta(0)\left(1 - e^{-\frac{r^2}{4vt}}\right) \tag{6}$$

As $t \to \infty$, the wake-induced velocity goes to zero. The Lamb-Oseen and Proctor models can be combined with Lamb wake age model to give a spatio-temperal distribution of the wake-induced downwash as

$$v_\theta = \frac{\Gamma_0}{2\pi r}\left[1 - e^{-\alpha_L\left(\frac{r}{r_c}\right)^2}\right]\left(1 - e^{-\frac{r^2}{4vt}}\right) \tag{7}$$

$$w_w = \begin{cases} \frac{\Gamma_0}{2\pi r}\left[1 - e^{-10\left(\frac{r_c}{b}\right)^{0.75}}\right]\left[\frac{1-e^{-\alpha_L\left(\frac{r}{r_c}\right)^2}}{1-e^{-\alpha_L(1.4)^2}}\right]\left(1 - e^{-\frac{r^2}{4vt}}\right) & r \le 1.4r_c \\ \frac{\Gamma_0}{2\pi r}\left[1 - e^{-10\left(\frac{|r|}{b}\right)^{0.75}}\right]\left(1 - e^{-\frac{r^2}{4vt}}\right) & r > 1.4r_c \end{cases} \tag{8}$$

The core radius depends on the type of aircraft. A study which involves flight measurements of the wake vortex core size behind a B757 aircraft indicates that the core size is about 1.4% of the wing span with a maximum downwash of 35 m/sec.[13] This study also indicates that many numerical wake vortex simulations tend to use a much larger core radius of up to 14%. As the core size reduces, the wake vortex intensity becomes greater. It is of interest to compare the downwash computed by the Lamb-Oseen and Proctor wake vortex models to the flight measurements for a B-757 aircraft. A typical operating weight of a B-757 aircraft is 200,000 lb. During landing, a typical approach speed is about 137 knots or 231 ft/sec. Based on this, the lift coefficient C_L at landing is obtained by

$$C_L = \frac{W}{\bar{q}S} \tag{9}$$

where W is the aircraft gross weight, $\bar{q}$ is the dynamic pressure, and S is the reference wing surface area which is 1951 ft^2 for B-757. The lift coefficient at approach is computed to be 1.6128 which is a large value as the aircraft is in a high-lift configuration with the flaps and slats fully deployed. The lift circulation strength Γ_0 for an elliptical lift distribution can be estimated by

$$\Gamma_0 = \frac{2C_L VS}{\pi b} = \frac{4L}{\pi\rho Vb} \tag{10}$$

where V is the airspeed and ρ is the air density. The lift distribution during an approach is most likely not an elliptical distribution. This may result in a higher lift circulation strength, but the effect might be assumed negligible. The lift circulation strength Γ_0 is computed to be 3720.4 ft^2/sec^2. Figure 7 is a plot that compares the Lamb-Oseen and Proctor wake vortex models to the flight measurement data extracted from Reference.[13] As can be seen, the Lamb-Oseen wake vortex model over-predicts the maximum downwash substantially. This is not surprising since it does not account for the wing span as in the Proctor wake vortex model. The Lamb-Oseen wake vortex model, on the other hand, estimates the far-field downwash with reasonable accuracy. The Proctor wake vortex model does a very good job of predicting the downwash.

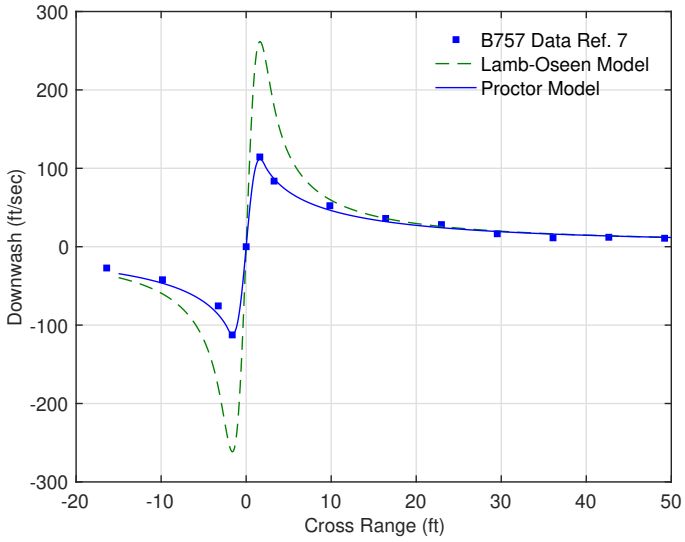

Figure 7. Comparison of Lamb-Oseen and Proctor Models to B757 Flight Data

For aircraft flying in the wake, the lift distribution is not necessarily symmetric between the left wing and right wing. To account for the lift asymmetry, the total lift circulation is split into the lift circulations of the individual wings. Thus, the individual lift circulations are expressed as

$$\Gamma_{0_{L,R}} = \frac{2L_{L,R}}{\pi\rho V b} \tag{11}$$

where the subscripts L and R denote the left wing and right wing.

C. Wake Age and Propagation

The wake age affects both the wake vortex core and the viscous dissipation simultaneously. Figure 8 plots the maximum amplitude of the wake-induced downwash as a function of time with only the wake vortex core growth and with the atmospheric dissipation in addition. As can be seen, the wake vortex decay is very slow and appears to be physically unrealistic. In reality, there are many conditions that affect wake vortex decay. Advection by winds is one effect on the wake vortex decay. In practice, wake vortices dissipate on timescales of seconds to minutes. The Lamb-Oseen wake vortex growth and viscous dissipation models are based on a simple diffusion model which predicts the wake vortex decay over a much longer timescale. The diffusion of wake vortices is almost never observed in practice.[14] A more realistic wake vortex decay model is thus needed.

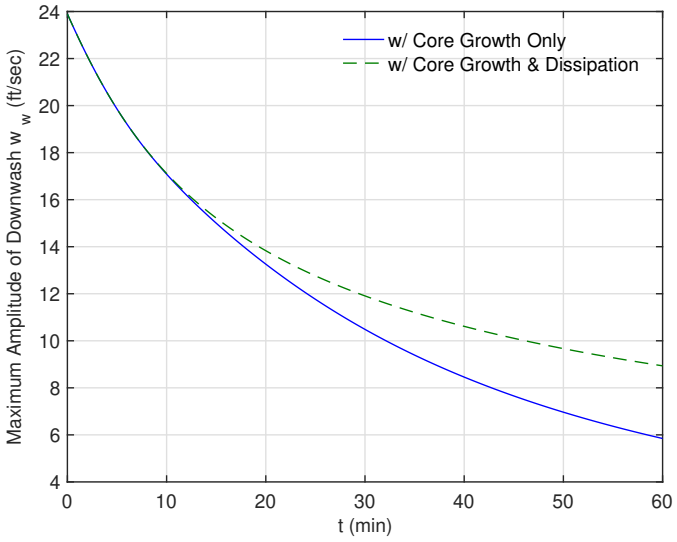

24

Figure 8. Wake Vortex Aging Effect on Downwash of Fixed Wing Aircraft A

Proctor et al. develop a three-phase vortex decay model within turbulent and stratified atmospheres using a large eddy simulation model to simulate the out-of-ground effect behavior of wake vortices due to their interaction with atmospheric turbulence and thermal stratification.[6] The results of this study are used to improve the wake age effect for use in our wake vortex interaction modeling. The three-phase wake decay model delineates the three zones of wake decay. During phase 1, the wing tip vortices are almost two-dimensional with very little variation in the longitudinal direction. The wake characteristic during phase 1 can be idealized by the Proctor or Lamb-Oseen model. During phase 2, the two wing tip vortices begin to link together. The wake decay during phase 2 occurs at a much faster rate than during phase 1. Phase 3 is characterized by a vortex ring structure when the wake decay rate begins to slow down. The three-phase wake decay model is presented for three different turbulence eddy dissipation rates, $\varepsilon^* = 0.03$, $\varepsilon^* = 0.15$, and $\varepsilon^* = 0.5$ in neutral atmosphere. Except for $\varepsilon^* = 0.5$, the three-phase wake decay model could be characterized by three linear decay models for the three phases. The phase 3 decay for $\varepsilon^* = 0.03$ exhibits a complex pattern that is far from a linear idealization. Based on the results of the Proctor's three-phase vortex decay model, this study proposes a simplified exponential decay model which is more appropriate for long-time horizon as the linear model suggested by Proctor predicts zero lift circulation strength at a finite time.

The proposed wake decay model is described by

$$\Gamma(t) = \Gamma_0 e^{-\alpha T} \tag{12}$$

where α is a wake age parameter obtained from curve-fitting the Proctor's wake decay simulation data[6] and T_i is the non-dimensional time which is related to the physical time as

$$T = \frac{tV_0}{b_0} \tag{13}$$

with

$$V_0 = \frac{\Gamma_0}{2\pi b_0} \tag{14}$$

and

$$b_0 = \frac{\pi b}{4} \tag{15}$$

Three different curve-fitting schemes are carried out: 1) curve-fitting only phase 1 simulation data, 2) curve-fitting both phase 1 and phase 2 data, and 3) curve-fitting all three phases. It is determined that curve-fitting only phase 1 data would provide more conservatism in the wake decay model. The conservatism is deemed necessary since a simplified model is used.

The wake age parameter α is estimated using the linear regression equation

$$\alpha = -\frac{\sum_{i=1}^{N} T_i \ln y_i}{\sum_{i=1}^{N} T_i^2} \tag{16}$$

where y_i is the normalized circulation from the Proctor's phase 1 data

The results of the curve-fitting are presented in Figure 9. The wake aging parameter α as a function of the non-dimensional eddy dissipation parameter ε^* is presented in Table 1.

ε^*	α
0.03	0.04887
0.15	0.06896
0.5	0.17929

Table 1. Parameter α for Wake Age Model

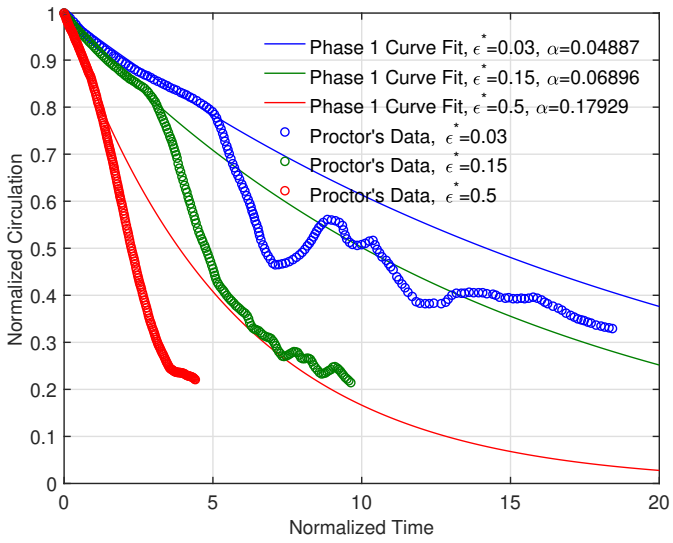

Figure 9. Wake Aging Model

The wake age parameter α can be modeled as a polynomial function of the eddy dissipation parameter ε^* as

$$\alpha = 0.3146\varepsilon^{*2} + 0.1108\varepsilon^* + 0.0453 \tag{17}$$

The wake age effect describes the temporal dissipation of wake vortices. We characterize wake propagation as a spatial dissipation at a given time. Typically, the wake-induced downwash remains nearly constant for some distance downstream of the wing tip vortex location. For example, flight test data obtained from a B-747 aircraft indicates that the near wake remains almost constant for about 32 wing spans. To model the spatial wake propagation, we choose a simplified exponential model

$$\Gamma(\Delta x) = \Gamma_0 e^{-\beta \Delta x} \tag{18}$$

where Δx is the relative distance from the aircraft that sheds wake vortices and β is a wake propagation parameter that can be suitably chosen. We combine both the Proctor simplified wake age model and wake propagation model to describe the spatial and temporal dissipation of the wake vortices. This is given by

$$\Gamma(\Delta x, t) = \Gamma(\Delta x)\, e^{-\frac{\alpha \Gamma(x) t}{2\pi b_0^2}} \tag{19}$$

This model enables the evolution of the wake-induced downwash as a function of time at any point in space.

D. Wake Vortex Model of Rotorcraft

Wake vortices shed by rotorcraft are much more complex due to the rotor wake interaction. The literature on wake vortices for rotorcraft gives a less clear picture of wake vortex models for rotorcraft than for fixed-wing aircraft. The rotor acts as a aircraft wing in forward flight. Thus, rolled-up vortices are also shed by the rotor at the rotor tips. Unlike fixed-wing aircraft, the lift circulation strength of a rotorcraft varies circumferentially. This implies that the downwash varies as a function of the azimuth angle of the rotor. The complex flow field near a rotor makes it difficult to develop a good understanding of the near field and far field wake behaviors. In the present analysis, we attempt to develop an analytical lift circulation model of a rotor in order to estimate its wake effects in a first-order approximation. In our model, we include the blade flapping motion as well as the cyclic pitch control to reduce lift asymmetry in a rotor.

The airspeed that the rotor blades see varies circumferentially as a function of the azimuth angle Ψ as shown in Figure 10. The tangential component of the relative velocity experienced by the rotor blades is

$$V_t = r\Omega + V\cos\alpha\sin\Psi \approx r\Omega + V\sin\Psi \tag{20}$$

where α is the angle of attack which is assumed to be small, $R_0 \le r \le R$, and R_0 is the hub radius.

The vertical component of the relative velocity is

$$V_z = V\sin\alpha \approx V\alpha \tag{21}$$

The radial component of the relative velocity is

$$V_r = V\cos\alpha\cos\Psi \approx V\cos\Psi \tag{22}$$

The magnitude of the normal relative velocity that generates the rotor lift is computed as

$$V_R = \sqrt{V_t^2 + V_z^2} = \sqrt{(r\Omega + V\sin\Psi)^2 + V^2\alpha^2} \tag{23}$$

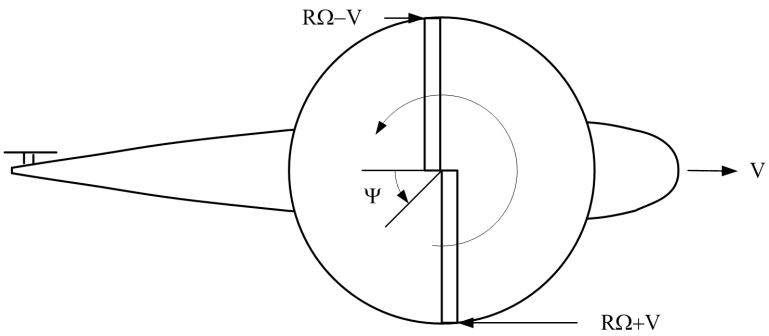

Figure 10. Rotor Velocities of Rotorcraft in Forward Flight

In the following analysis, we assume a rigid rotor which does not account for the flapping motion of the rotor blades. Later on, we will account for the flapping motion of the rotor blades. We assume that the rotor has a constant chord c and the rotor blade section is a symmetric airfoil. If we assume $\alpha \approx 0$, $R_0 \approx 0$, and the flow is essentially incompressible at low tip speeds, then the lift produced by the rotor blades is computed as

$$L = N\rho\int_0^R V_R\Gamma dr \approx N\rho\int_0^R (r\Omega + V\sin\Psi)\Gamma dr \tag{24}$$

where N is the number of blades.

Using the lifting line theory, we express the lift circulation in terms of the Fourier sine series as

$$\Gamma = 4RV\sum_{n=1}^{m} A_n \sin n\psi \tag{25}$$

where the Fourier coefficients A_n are given by

$$A_n = \frac{1}{2\pi RV}\int_0^\pi \Gamma \sin n\psi d\psi \tag{26}$$

and ψ is related to r as

$$2r = R - R\cos\psi \tag{27}$$

The lift is then obtained as

$$\begin{aligned} L &= 2N\rho R^2 V \int_0^\pi \left(\frac{R - R\cos\psi}{2}\Omega + V\sin\Psi\right)\sum_{n=1}^{m} A_n \sin n\psi \sin\psi d\psi \\ &= 2N\rho R^2 V \left[\left(\frac{R\Omega}{2} + V\sin\Psi\right)\frac{A_1\pi}{2} - \frac{R\Omega}{4}\frac{A_2\pi}{2}\right] \\ &= \pi N\rho R^3 \Omega V \left[\left(\frac{1}{2} + \mu\sin\Psi\right)A_1 - \frac{1}{4}A_2\right] \end{aligned} \tag{28}$$

If we assume the elliptical lift circulation

$$\Gamma = \Gamma_0\sqrt{1 - \left(\frac{r}{R}\right)^2} = \Gamma_0\sqrt{1 - \frac{1}{4}(1-\cos\psi)^2} \tag{29}$$

then A_1 and A_2 are evaluated as

$$A_1 = \frac{\Gamma_0}{2\pi RV}\int_0^\pi \sqrt{1 - \frac{1}{4}(1-\cos\psi)^2}\sin\psi d\psi = \frac{\Gamma_0}{4RV} \tag{30}$$

$$A_2 = \frac{\Gamma_0}{2\pi RV}\int_0^\pi \sqrt{1 - \frac{1}{4}(1-\cos\psi)^2}\sin 2\psi d\psi = \frac{\Gamma_0}{2\pi RV}\left(\pi - \frac{8}{3}\right) \tag{31}$$

Therefore, we obtain

$$L = N\rho\Gamma_0 R^2\Omega\left(\frac{1}{3} + \frac{\pi}{4}\mu\sin\Psi\right) \tag{32}$$

where $\mu = \dfrac{V}{R\Omega}$ is the advance ratio.

The mean lift is obtained by integrating L over the entire revolution which yields

$$\bar{L} = \frac{1}{2\pi}\int_0^{2\pi} L d\Psi = \frac{1}{3}N\rho\Gamma_0 R^2\Omega \tag{33}$$

If the mean lift balances the weight W of the rotorcraft, then the mean lift circulation strength of a rotor blade is obtained as

$$\bar{\Gamma}_0 = \frac{3W}{N\rho R^2\Omega} \tag{34}$$

The instantaneous lift circulation strength is equal to

$$\Gamma_0 = \frac{12W}{N\rho R^2\Omega(4 + 3\pi\mu\sin\Psi)} \tag{35}$$

Thus, the lift varies as a function of the azimuth angle. It reaches the maximum value on the advancing side where $\Psi = 90^\circ$ and the minimum value on the retreating side where $\Psi = 270^\circ$. This results in a lift asymmetry that tends to generate a rolling moment. The mean rolling moment is computed as

$$\begin{aligned} \bar{l} &= -\frac{N}{2\pi}\int_0^{2\pi}\int_0^R \rho V_R \Gamma r\sin\Psi dr d\Psi = -\frac{N\rho\Gamma_0}{2\pi}\int_0^{2\pi}\int_0^R (r\Omega + V\sin\Psi)\sqrt{1 - \left(\frac{r}{R}\right)^2}\, r\sin\Psi dr d\Psi \\ &= -\frac{1}{2}N\rho\Gamma_0 V\int_0^R \sqrt{1 - \left(\frac{r}{R}\right)^2}\, r dr = -\frac{1}{6}N\rho\Gamma_0 V R^2 \end{aligned} \tag{36}$$

In the analysis heretofore, the blade flapping motion as well as cyclic pitch control in forward flight have not been considered. The blade flapping motion alleviates the lift symmetry due to the offsetting lift resulting from the blade flapping motion. Consider a plunging airfoil with downward or plunge displacement h subject to an incoming airspeed V_R. The plunging airfoil can be used to model the blade flapping motion at a blade radial distance. The lift force generates an upward displacement due to the articulated hinge. This upward displacement varies as a function of the azimuth angle. Assuming a rigid-body blade flapping motion, then the plunge displacement is linearly varying with the blade radius as

$$h = -r\beta \tag{37}$$

where β is the blade flapping angle, positive upward, and the negative sign indicates the upward plunge displacement. The plunge velocity $\dot{h}$ creates an effective angle of attack. The blade flapping motion also creates an induced normal velocity component due to the forward airspeed velocity in the radial direction. Thus, the combined effective angle of attack due to the blade flapping motion is given by

$$\alpha_f = -\frac{V\beta\cos\Psi}{V_R} + \frac{\dot{h}}{V_R} \tag{38}$$

The blade pitch control is used to control the rotor lift by changing the blade pitch angle to generate lift on a rotor. The unsteady lift can be modeled by the Theodorsen's theory[15] which shows that the unsteady lift of an airfoil is comprised of two components: a circulatory lift and a non-circulatory lift. The circulatory lift coefficient is given by

$$c_{l_c} = C(k)\, c_{l_\alpha}\left(\alpha_f + \theta + \frac{e_c\dot{\theta}}{V_R}\right) = C(k)\, c_{l_\alpha}\left(\theta + \frac{e_c\dot{\theta}}{V_R} - \frac{V\beta\cos\Psi}{V_R} - \frac{r\dot{\beta}}{V_R}\right) \tag{39}$$

where θ is the blade pitch angle, e_c is the offset between the pitch center and the three-quarter chord point, $\dot{h}$ is the plunge or blade flapping velocity which is positive in the downward direction, and $C(k)$ is the complex-valued Theodorsen's function[15] given by

$$C(k) = F(k) + iG(k) \tag{40}$$

The functions $F(k)$ and $G(k)$ represent the amplitude and phase corrections of the steady lift, respectively. They are shown in Figure 11. The reduced frequency k is defined as

$$k = \frac{\omega c}{2V_R} \tag{41}$$

where ω is the frequency of the airfoil oscillation and c is the airfoil chord. The value of the function $F(k)$ is always less than 1 which represents the lift reduction in unsteady flow and tends to $\frac{1}{2}$ as $k \to \infty$. When $k = 0$, the flow is steady. This corresponds to $F(0) = 1$ and $G(0) = 0$. The value of the function $G(k)$ is negative which indicates a phase lag as the lift circulation cannot be established instantaneously in response to the sinusoidal angle of attack. If the blade flapping motion and pitch angle are periodic at the one-per-revolution frequency Ω, the reduced frequency can be approximated by $k \approx \dfrac{c}{2R}$ and the circulatory lift coefficient can be expressed as

$$\begin{aligned} c_{l_c} =& F(k)\, c_{l_\alpha}\left(\theta + \frac{e_c\dot{\theta}}{V_R} - \frac{V\beta\cos\Psi}{V_R} - \frac{r\dot{\beta}}{V_R}\right) \\ &+ G(k)\, c_{l_\alpha}\left(\frac{\dot{\theta}}{\Omega} + \frac{e_c\ddot{\theta}}{\Omega V_R} - \frac{V\dot{\beta}\cos\Psi}{\Omega V_R} + \frac{V\beta\sin\Psi}{V_R} - \frac{r\ddot{\beta}}{\Omega V_R}\right) \end{aligned} \tag{42}$$

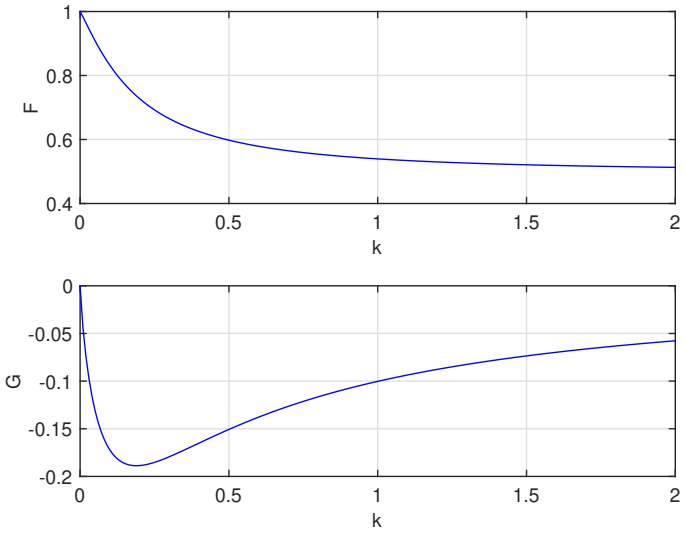

Figure 11. Theodorsen's Function

The non-circulatory lift is due to the inertial force acting on the airfoil, also known as the apparent mass effect. The non-circulatory lift coefficient given by

$$c_{l_{nc}} = c_{l_\alpha}\left(\frac{c\dot{\theta}}{4V_R} + \frac{e_m c\ddot{\theta}}{4V_R^2} + \frac{c\ddot{h}}{4V_R^2}\right) = c_{l_\alpha}\left(\frac{c\dot{\theta}}{4V_R} + \frac{e_m c\ddot{\theta}}{4V_R^2} - \frac{c\ddot{\beta}r}{4V_R^2}\right) \tag{43}$$

where e_m is the offset between the pitch center and the mid-chord point.

The total lift is equal to the steady-state lift plus the circulatory lift and non-circulatory lift

$$\begin{aligned}\tilde{c}_l =& c_l + F(k)\, c_{l_\alpha}\left(\theta + \frac{e_c\dot{\theta}}{V_R} - \frac{V\beta\cos\Psi}{V_R} - \frac{r\dot{\beta}}{V_R}\right)\\ &+ G(k)\, c_{l_\alpha}\left(\frac{\dot{\theta}}{\Omega} + \frac{e_c\ddot{\theta}}{\Omega V_R} - \frac{V\dot{\beta}\cos\Psi}{\Omega V_R} + \frac{V\beta\sin\Psi}{V_R} - \frac{r\ddot{\beta}}{\Omega V_R}\right)\\ &+ c_{l_\alpha}\left(\frac{c\dot{\theta}}{4V_R} + \frac{e_m c\ddot{\theta}}{4V_R^2} - \frac{c\ddot{\beta}r}{4V_R^2}\right)\end{aligned} \tag{44}$$

For simplification, we make a quasi-steady aerodynamics assumption for which $F(k) = 1$ and $G(k) = 0$. Then, the unsteady lift is approximated as

$$\tilde{c}_l = c_l + c_{l_\alpha}\left(\theta + \frac{e_c\dot{\theta}}{V_R} + \frac{c\dot{\theta}}{4V_R} + \frac{e_m c\ddot{\theta}}{4V_R^2} - \frac{V\beta\cos\Psi}{V_R} - \frac{r\dot{\beta}}{V_R} - \frac{c\ddot{\beta}r}{4V_R^2}\right) \tag{45}$$

The blade flapping angle can be computed by summing the moment about the hinge which gives

$$I\ddot{\beta} + K\beta = \rho\int_0^R V_R\left(\Gamma + \Gamma_c + \Gamma_{nc}\right) r dr - I\Omega^2\beta \tag{46}$$

where I is the blade moment of inertia about the axis of the flapping motion, K is the spring constant of the articulated hinge, and Γ_c and Γ_{nc} are the circulatory and non-circulatory lift circulations, respectively. The second term in the right hand side is the moment due to the centrifugal force.

The steady-state response of the blade flapping motion is at the same frequency of the steady-state lift at one-per-revolution frequency Ω. Therefore, the blade flapping angle can be expressed in the rotorcraft convention as

$$\beta = \beta_0 + \beta_{1s}\sin\Omega t + \beta_{1c}\cos\Omega t \tag{47}$$

where β_0 is the mean blade flapping angle, β_{1s} is the cyclic flapping amplitude of the one-per-revolution sine component, and β_{1c} is the cyclic flapping amplitude of the one-per-revolution cosine component

The pitch control is expressed similarly as

$$\theta = \theta_0 + \theta_{1s}\sin\Omega t + \theta_{1c}\cos\Omega t \tag{48}$$

where θ_0 is the collective pitch angle, θ_{1s} is the cyclic pitch amplitude of the one-per-revolution sine component, and θ_{1c} is the cyclic pitch amplitude of the one-per-revolution cyclic cosine component

Assuming the spring force of the hinge is zero, the radial moment, rolling moment, and pitching moment can be evaluated by the following equations:

$$\begin{aligned}\bar{M} &= \frac{1}{2\pi}\int_0^{2\pi}\int_0^R \rho V_R\left(\Gamma+\Gamma_c+\Gamma_{nc}\right) r dr d\Psi = \frac{1}{2\pi}\int_0^{2\pi}\left(I\ddot{\beta}+I\Omega^2\beta\right)d\Psi \\ &= \frac{1}{2\pi}\int_0^{2\pi} I\Omega^2\beta_0 d\Psi = I\Omega^2\beta_0\end{aligned} \tag{49}$$

$$\begin{aligned}\bar{l} &= -\frac{N}{2\pi}\int_0^{2\pi}\int_0^R \rho V_R\left(\Gamma+\Gamma_c+\Gamma_{nc}\right) r\sin\Psi dr d\Psi = -\frac{N}{2\pi}\int_0^{2\pi}\left(I\ddot{\beta}+I\Omega^2\beta\right)\sin\Psi d\Psi \\ &= -\frac{N}{2\pi}\int_0^{2\pi} I\Omega^2\beta_0\sin\Psi d\Psi = 0\end{aligned} \tag{50}$$

$$\begin{aligned}\bar{m} &= -\frac{N}{2\pi}\int_0^{2\pi}\int_0^R \rho V_R\left(\Gamma+\Gamma_c+\Gamma_{nc}\right) r\cos\Psi dr d\Psi = -\frac{N}{2\pi}\int_0^{2\pi}\left(I\ddot{\beta}+I\Omega^2\beta\right)\cos\Psi d\Psi \\ &= -\frac{N}{2\pi}\int_0^{2\pi} I\Omega^2\beta_0\cos\Psi d\Psi = 0\end{aligned} \tag{51}$$

where $\bar{M}$ is the mean radial moment and $\bar{m}$ is the mean pitching moment

The last two equations show that the inertial force and the centrifugal force cancel out, thereby resulting in zero rolling and pitching moments. Therefore, the blade flapping angle and blade pitch angle can be evaluated using the zero moment equations

$$\begin{aligned}&\frac{1}{2\pi}\int_0^{2\pi}\int_0^R \rho V_R\Gamma r dr d\Psi \\ &\quad+\frac{1}{2\pi}\int_0^{2\pi}\int_0^R \frac{1}{2}\rho V_R^2 c_{l_\alpha}\left(\theta+\frac{e_c\dot{\theta}}{V_R}+\frac{c\dot{\theta}}{4V_R}+\frac{e_m c\ddot{\theta}}{4V_R^2}-\frac{V\beta\cos\Psi}{V_R}-\frac{\dot{\beta}r}{V_R}-\frac{c\ddot{\beta}r}{4V_R^2}\right)c r dr d\Psi = I\Omega^2\beta_0\end{aligned} \tag{52}$$

$$\begin{aligned}&\frac{1}{2\pi}\int_0^{2\pi}\int_0^R \rho V_R\Gamma r\sin\Psi dr d\Psi \\ &\quad+\frac{1}{2\pi}\int_0^{2\pi}\int_0^R \frac{1}{2}\rho V_R^2 c_{l_\alpha}\left(\theta+\frac{e_c\dot{\theta}}{V_R}+\frac{c\dot{\theta}}{4V_R}+\frac{e_m c\ddot{\theta}}{4V_R^2}-\frac{V\beta\cos\Psi}{V_R}-\frac{\dot{\beta}r}{V_R}-\frac{c\ddot{\beta}r}{4V_R^2}\right)c r\sin\Psi dr d\Psi = 0\end{aligned} \tag{53}$$

$$\begin{aligned}&\frac{1}{2\pi}\int_0^{2\pi}\int_0^R \rho V_R\Gamma r\cos\Psi dr d\Psi \\ &\quad+\frac{1}{2\pi}\int_0^{2\pi}\int_0^R \frac{1}{2}\rho V_R^2 c_{l_\alpha}\left(\theta+\frac{e_c\dot{\theta}}{V_R}+\frac{c\dot{\theta}}{4V_R}+\frac{e_m c\ddot{\theta}}{4V_R^2}-\frac{V\beta\cos\Psi}{V_R}-\frac{\dot{\beta}r}{V_R}-\frac{c\ddot{\beta}r}{4V_R^2}\right)c r\cos\Psi dr d\Psi = 0\end{aligned} \tag{54}$$

Upon integration, we obtain

$$\begin{aligned}&\frac{\pi}{16}\rho\Gamma_0 R^3\Omega+\rho c_{l_\alpha}cR^4\Omega^2\left[\frac{1}{8}\left(1+\mu^2\right)\theta_0+\frac{1}{6}\mu\theta_{1s}-\frac{1}{8}\left(\frac{e_c}{R}+\frac{1}{4}\frac{c}{R}\right)\mu\theta_{1c}\right] \\ &\qquad = I\Omega^2\beta_0\end{aligned} \tag{55}$$

$$\frac{1}{6}\mu\rho\Gamma_0 R^3\Omega+\rho c_{l_\alpha}cR^4\Omega^2\left[\frac{1}{6}\mu\theta_0+\frac{1}{32}\left(2+3\mu^2-\frac{c}{R}\frac{e_m}{R}\right)\theta_{1s}-\frac{1}{12}\left(\frac{e_c}{R}+\frac{1}{4}\frac{c}{R}\right)\theta_{1c}\right]$$
$$+\rho c_{l_\alpha}cR^4\Omega^2\left[\frac{1}{48}\frac{c}{R}\beta_{1s}+\frac{1}{32}\left(2-\mu^2\right)\beta_{1c}\right]=0 \quad (56)$$

$$\rho c_{l_\alpha}cR^4\Omega^2\left[\frac{1}{12}\left(\frac{e_c}{R}+\frac{1}{4}\frac{c}{R}\right)\theta_{1s}+\frac{1}{32}\left(2+\mu^2-\frac{c}{R}\frac{e_m}{R}\right)\theta_{1c}\right]$$
$$-\rho c_{l_\alpha}cR^4\Omega^2\left[\frac{1}{12}\mu\beta_0+\frac{1}{32}\left(2+\mu^2\right)\beta_{1s}-\frac{1}{48}\frac{c}{R}\beta_{1c}\right]=0 \quad (57)$$

If the pitch center is at the quarter-chord location, then $e_c=\frac{c}{2}$ and $e_m=\frac{c}{4}$. For high aspect ratio rotor blades, $\frac{c}{R}<0.1$. Therefore, we can assume that these terms are negligible. This assumption leads to

$$\frac{1}{8}\left(1+\mu^2\right)\theta_0+\frac{1}{6}\mu\theta_{1s}-\frac{I}{\rho c_{l_\alpha}cR^4}\beta_0\approx-\frac{\pi\Gamma_0}{16c_{l_\alpha}cR\Omega} \quad (58)$$

$$\frac{1}{6}\mu\theta_0+\frac{1}{32}\left(2+3\mu^2\right)\theta_{1s}+\frac{1}{32}\left(2-\mu^2\right)\beta_{1c}\approx-\frac{\mu\Gamma_0}{6c_{l_\alpha}cR\Omega} \quad (59)$$

$$\theta_{1c}-\frac{8\mu}{3\left(2+\mu^2\right)}\beta_0-\beta_{1s}=0 \quad (60)$$

To eliminate the lift asymmetry so that the rotor thrust is uniform, we require the instantaneous lift to be equal to the mean lift

$$L=N\int_0^R\rho V_R\left(\Gamma+\Gamma_c+\Gamma_{nc}\right)dr=\bar{L} \quad (61)$$

Retaining only the mean and first harmonic components, we obtain

$$L\approx A_0+A_{1s}\sin\Psi+A_{1c}\cos\Psi=\frac{N}{3}\rho\Gamma_0R^2\Omega \quad (62)$$

where

$$A_0=\frac{1}{2\pi}\int_0^{2\pi}Ld\Psi=\frac{N}{3}\rho\Gamma_0R^2\Omega+\frac{N}{2}\rho c_{l_\alpha}cR^3\Omega^2\left[\left(\frac{1}{3}+\frac{1}{2}\mu^2\right)\theta_0+\frac{1}{2}\mu\theta_{1s}-\frac{1}{2}\left(\frac{e_c}{R}+\frac{1}{4}\frac{c}{R}\right)\mu\theta_{1c}\right] \quad (63)$$

$$\begin{aligned}A_{1s}=&\frac{1}{\pi}\int_0^{2\pi}L\sin\Psi d\Psi\\=&N\rho\Gamma_0R^2\Omega\frac{\pi}{4}\mu\\&+\frac{N}{2}\rho c_{l_\alpha}cR^3\Omega^2\left[\mu\theta_0+\left(\frac{1}{3}+\frac{3}{4}\mu^2-\frac{1}{4}\frac{c}{R}\frac{e_m}{R}\right)\theta_{1s}-\frac{1}{2}\left(\frac{e_c}{R}+\frac{1}{4}\frac{c}{R}\right)\theta_{1c}+\left(\frac{1}{3}-\frac{1}{4}\mu^2\right)\beta_{1c}+\frac{1}{8}\frac{c}{R}\beta_{1s}\right]\end{aligned} \quad (64)$$

$$\begin{aligned}A_{1c}=&\frac{1}{\pi}\int_0^{2\pi}L\cos\Psi d\Psi\\=&\frac{N}{2}\rho c_{l_\alpha}cR^3\Omega^2\left[\left(\frac{1}{3}+\frac{1}{4}\mu^2-\frac{1}{4}\frac{c}{R}\frac{e_m}{R}\right)\theta_{1c}-\frac{1}{2}\mu\beta_0-\left(\frac{1}{3}+\frac{1}{4}\mu^2\right)\beta_{1s}+\frac{1}{2}\left(\frac{e_c}{R}+\frac{1}{4}\frac{c}{R}\right)\theta_{1s}+\frac{1}{8}\frac{c}{R}\beta_{1c}\right]\end{aligned} \quad (65)$$

The terms A_0 and A_{1s} are matched which yields

$$\left(\frac{1}{3}+\frac{1}{2}\mu^2\right)\theta_0+\frac{1}{2}\mu\theta_{1s}-\frac{1}{2}\left(\frac{e_c}{R}+\frac{1}{4}\frac{c}{R}\right)\mu\theta_{1c}=0 \quad (66)$$

$$\mu\theta_0+\left(\frac{1}{3}+\frac{3}{4}\mu^2-\frac{1}{4}\frac{c}{R}\frac{e_m}{R}\right)\theta_{1s}-\frac{1}{2}\left(\frac{e_c}{R}+\frac{1}{4}\frac{c}{R}\right)\theta_{1c}+\frac{1}{8}\frac{c}{R}\beta_{1s}+\left(\frac{1}{3}-\frac{1}{4}\mu^2\right)\beta_{1c}=-\frac{\pi\mu\Gamma_0}{2c_{l_\alpha}cR\Omega} \tag{67}$$

If we neglect the terms $\frac{c}{R}$,$\frac{e_c}{R}$, and $\frac{e_m}{R}$, these equations can be approximated as

$$\left(\frac{1}{3}+\frac{1}{2}\mu^2\right)\theta_0+\frac{1}{2}\mu\theta_{1s}\approx 0 \tag{68}$$

$$\mu\theta_0+\left(\frac{1}{3}+\frac{3}{4}\mu^2\right)\theta_{1s}+\left(\frac{1}{3}-\frac{1}{4}\mu^2\right)\beta_{1c}\approx-\frac{\pi\mu\Gamma_0}{2c_{l_\alpha}cR\Omega} \tag{69}$$

Setting $\theta_{1c}=0$ since the cosine component of the cyclic pitch control is usually small and neglecting higher order terms of μ, we obtain the following approximate solutions for θ_0, θ_{1s}, β_0, β_{1s}, and β_{1c}:

$$\theta_0=\frac{\left[9\pi\left(2+5\mu^2\right)-8\left(4+9\mu^2\right)\right]\Gamma_0}{2\left(2+9\mu^2\right)c_{l_\alpha}cR\Omega} \tag{70}$$

$$\theta_{1s}=-\frac{\left[9\pi\left(2+5\mu^2\right)-8\left(4+9\mu^2\right)\right]\Gamma_0}{6\mu\left(1+3\mu^2\right)c_{l_\alpha}cR\Omega} \tag{71}$$

$$\beta_0=\frac{\left[9\pi\left(1+5\mu^2\right)-2\left(4+9\mu^2\right)\right]\rho\Gamma_0R^3}{36\left(2+15\mu^2\right)I\Omega} \tag{72}$$

$$\beta_{1c}=\frac{\left[9\pi\left(2+\mu^2\right)-8\left(4+3\mu^2\right)\right]\Gamma_0}{6\mu\left(1+3\mu^2\right)c_{l_\alpha}cR\Omega} \tag{73}$$

$$\beta_{1s}=-\frac{\left[9\pi\left(1+5\mu^2\right)-2\left(4+9\mu^2\right)\right]\mu\rho\Gamma_0R^3}{54\left(1+8\mu^2\right)I\Omega} \tag{74}$$

The lift equation now only contains the small A_{1c} harmonic cosine component and higher harmonic terms

$$L=N\rho\Gamma_0R^2\Omega\left[\frac{1}{3}-\frac{\left[9\pi\left(2+7\mu^2\right)-4\left(4+3\mu^2\right)\right]\mu\rho c_{l_\alpha}cR^4}{5184\left(1+8\mu^2\right)I}\cos\Psi+\cdots\right] \tag{75}$$

The ratio $\frac{\rho c_{l_\alpha}cR^4}{I}$ is called the Lock number and is usually 8 to 10 for articulated rotors. Thus, the largest value of the cosine term is about 0.07μ. Hence, the lift asymmetry which creates a rolling moment is eliminated by the blade flapping motion and blade pitch control. The remaining terms are small and the lift circulation strength can be obtained as

$$\Gamma_0\approx\frac{3W}{N\rho\Gamma_0R^2\Omega} \tag{76}$$

Using this lift circulation strength, the Proctor wake vortex model may be used to estimate the wake-induced downwash of rotorcraft. An analytical model of a wake vortex core size for helicopters shows that that the core size varies with the blade azimuth angle Ψ and ranges from 4% of the rotor radius at $\Psi=270^\circ$ corresponding to the minimum velocity at the retreating blade tip to 7.5% of the rotor radius at $\Psi=90^\circ$ corresponding to the maximum velocity at the advancing blade tip.[16] The study suggests an average wake vortex core radius of 5%. Another CFD study of rotor blade wake vortices shows an nearly equal lift circulation strength on the advancing side and retreating side when the blade flapping motion and cyclic pitch control are taken into account.[17]

E. Wake Vortex Interaction

The location where the wake-induced velocity is computed is denoted by the coordinate (x_c,y_c,z_c) in the NED (North East Down) inertial reference frame. The aircraft center of gravity (CG) is denoted by the coordinate (x,y,z) in the inertial reference frame. The aircraft CG moves with the aircraft according to

$$\begin{bmatrix} \dot{x} \\ \dot{y} \\ \dot{z} \end{bmatrix} = \begin{bmatrix} \cos\theta\cos\psi & -\cos\phi\sin\psi+\sin\phi\sin\theta\cos\psi & \sin\phi\sin\psi+\cos\phi\sin\theta\cos\psi \\ \cos\theta\sin\psi & \cos\phi\cos\psi+\sin\phi\sin\theta\sin\psi & -\sin\phi\cos\psi+\cos\phi\sin\theta\sin\psi \\ -\sin\theta & \sin\phi\cos\theta & \cos\phi\cos\theta \end{bmatrix} \begin{bmatrix} u \\ v \\ w \end{bmatrix} \tag{77}$$

The coordinate of the wing tip is related to the aircraft CG by the following coordinate transformation. The aircraft velocity components (u,v,w) and angular rates (p,q,r) are defined relative to the body-fixed reference frame with a coordinate system (x_b,y_b,z_b) whose origin is attached to the aircraft CG as shown in Figure 12. The equations of motion of the aircraft are to be established for the non-rotating earth-fixed inertial reference frame.

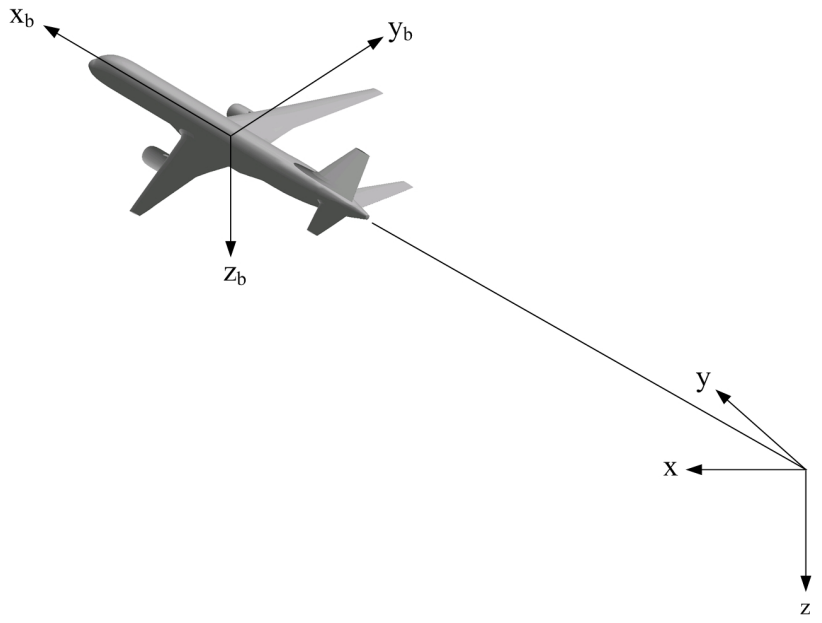

Figure 12. Inertial and Aircraft Body-Fixed Reference Frames

Consider the unit vectors $(\mathbf{i},\mathbf{j},\mathbf{k})$ attached to the inertial reference frame and the unit vectors $(\mathbf{i}_b,\mathbf{j}_b,\mathbf{k}_b)$ attached to the aircraft body-fixed reference frame. The inertial reference frame and the aircraft body-fixed reference frame are related by

$$\begin{bmatrix} \mathbf{i} \\ \mathbf{j} \\ \mathbf{k} \end{bmatrix} = \begin{bmatrix} \cos\theta\cos\psi & -\cos\phi\sin\psi+\sin\phi\sin\theta\cos\psi & \sin\phi\sin\psi+\cos\phi\sin\theta\cos\psi \\ \cos\theta\sin\psi & \cos\phi\cos\psi+\sin\phi\sin\theta\sin\psi & -\sin\phi\cos\psi+\cos\phi\sin\theta\sin\psi \\ -\sin\theta & \sin\phi\cos\theta & \cos\phi\cos\theta \end{bmatrix} \begin{bmatrix} \mathbf{i}_b \\ \mathbf{j}_b \\ \mathbf{k}_b \end{bmatrix} \tag{78}$$

Assuming the wing tip and the aircraft CG are at the same x_b and z_b coordinates. The wing tip coordinate in the body-fixed reference frame is

$$\mathbf{r}_t = \pm\frac{b}{2}\mathbf{j}_b \tag{79}$$

In the body-fixed reference frame, the wake-induced location is expressed as

$$\begin{aligned} \mathbf{r}_c = {} & (\Delta x_c\cos\theta\cos\psi+\Delta y_c\cos\theta\sin\psi-\Delta z_c\sin\theta)\,\mathbf{i}_b \\ & +[\Delta x_c(-\cos\phi\sin\psi+\sin\phi\sin\theta\cos\psi)+\Delta y_c(\cos\phi\cos\psi+\sin\phi\sin\theta\sin\psi)+\Delta z_c\sin\phi\cos\theta]\,\mathbf{j}_b \\ & +[\Delta x_c(\sin\phi\sin\psi+\cos\phi\sin\theta\cos\psi)+\Delta y_c(-\sin\phi\cos\psi+\cos\phi\sin\theta\sin\psi)+\Delta z_c\cos\phi\cos\theta]\,\mathbf{k}_b \end{aligned} \tag{80}$$

where

$$\begin{bmatrix} \Delta x_c \\ \Delta y_c \\ \Delta z_c \end{bmatrix} = \begin{bmatrix} x \\ y \\ z \end{bmatrix} - \begin{bmatrix} x_c \\ y_c \\ z_c \end{bmatrix} \tag{81}$$

The vector of the wake-induced location relative to the wing tip is expressed as

$$\Delta\mathbf{r} = \mathbf{r}_c - \mathbf{r}_t = \Delta x\mathbf{i}_b + \left(\Delta y \mp \frac{b}{2}\right)\mathbf{j}_b + \Delta z\mathbf{k}_b \tag{82}$$

where

$$\begin{bmatrix} \Delta x \\ \Delta y \\ \Delta z \end{bmatrix} = \begin{bmatrix} \Delta x_c \cos\theta\cos\psi + \Delta y_c \cos\theta\sin\psi - \Delta z_c \sin\theta \\ \Delta x_c\left(-\cos\phi\sin\psi + \sin\phi\sin\theta\cos\psi\right) + \Delta y_c\left(\cos\phi\cos\psi + \sin\phi\sin\theta\sin\psi\right) + \Delta z_c \sin\phi\cos\theta \\ \Delta x_c\left(\sin\phi\sin\psi + \cos\phi\sin\theta\cos\psi\right) + \Delta y_c\left(-\sin\phi\cos\psi + \cos\phi\sin\theta\sin\psi\right) + \Delta z_c\cos\phi\cos\theta \end{bmatrix} \tag{83}$$

The wake-induced downwash is computed by the Proctor model[11] as

$$w_w = \begin{cases} \frac{\Gamma(t)}{2\pi r}\left[1 - e^{-10\left(\frac{1.4r_c}{b}\right)^{0.75}}\right]\left[\frac{1-e^{-\alpha_L\left(\frac{r}{r_c}\right)^2}}{1-e^{-\alpha_L(1.4)^2}}\right] & r \le 1.4r_c \\ \frac{\Gamma(t)}{2\pi r}\left[1 - e^{-10\left(\frac{|r|}{b}\right)^{0.75}}\right] & r > 1.4r_c \end{cases} \tag{84}$$

where $\alpha_L = 1.25643$,

$$r^2 = \left(\Delta y \mp \frac{b}{2}\right)^2 + \Delta z^2 \tag{85}$$

and $\Gamma(t)$ is given by the wake age model given by Eq. (12).

During a maneuvering flight, the motion of an aircraft requires a constantly changing lift circulation strength which depends on the lift coefficient. Considering two types of maneuvering flight: 1) a maneuvering flight in the vertical plane, and 2) a turning flight. Both of the flight maneuvers cause the lift circulation strength to change and that must be taken into account in the wake vortex interaction model.

1. Maneuvering Flight in Vertical Plane

The equations of motion of an aircraft in non-rotating flat earth are given by

$$\dot{x} = V\cos\gamma\cos\psi \tag{86}$$

$$\dot{y} = V\cos\gamma\sin\psi \tag{87}$$

$$\dot{h} = V\sin\gamma \tag{88}$$

$$\dot{V} = \frac{T\cos\alpha - D - W\sin\gamma}{m} \tag{89}$$

$$\dot{\gamma} = \frac{T\sin\alpha + L\cos\phi - W\cos\gamma}{mV} \tag{90}$$

$$\dot{\psi} = \frac{L\sin\phi}{mV\cos\gamma} \tag{91}$$

where γ is the flight path angle, ψ is the heading angle, ϕ is the bank angle, x is the distance in the northerly direction, y is the distance in the easterly direction, h is the altitude, T is the engine thrust, D is the drag force, L is the lift force, W is the aircraft weight, V is the airspeed, and m is the aircraft mass.

The lift coefficient is computed as

$$C_L = \frac{L}{\bar{q}S} \tag{92}$$

where $\bar{q} = \frac{1}{2}\rho(h)V^2$ is the dynamic pressure and S is the wing reference area. The lift coefficient is related to the angle of attack as

$$C_L = C_{L_0} + C_{L_\alpha}\alpha \tag{93}$$

The drag coefficient is given by a parabolic drag polar

$$C_D = C_{D_0} + KC_L^2 \tag{94}$$

If we restrict the aircraft motion in a vertical plane for symmetric flight only, then $\psi = 0$, $\phi = 0$, and

$$\dot{x} = V\cos\gamma \tag{95}$$

$$\dot{y} = 0 \tag{96}$$

$$\dot{h} = V\sin\gamma \tag{97}$$

$$\dot{V} = \frac{T\cos\alpha - D - W\sin\gamma}{m} \tag{98}$$

$$\dot{\gamma} = \frac{T\sin\alpha + L - W\cos\gamma}{mV} \tag{99}$$

$$\dot{\psi} = 0 \tag{100}$$

If a flight maneuver is prescribed by the flight path angle $\gamma(t)$ and $V(t)$ in the vertical plane, then we can compute $\dot{\gamma}(t)$ and $\dot{V}(t)$ as well as $h(t)$. The engine thrust and lift coefficient can be computed from

$$T = \frac{m\dot{V} + \frac{1}{2}\rho(h)V^2S\left(C_{D_0} + KC_L^2\right) + W\sin\gamma}{\cos\alpha} \tag{101}$$

$$C_L = \frac{2\left(mV\dot{\gamma} - T\sin\alpha + W\cos\gamma\right)}{\rho(h)V^2S} \tag{102}$$

These equations are nonlinear since α depends on C_L and h depends on γ and V. To simplify the computation, we make a small angle assumption that $\alpha \approx 0$ and $\gamma \approx 0$. Then, the equations above are simplified to

$$T \approx m\dot{V} + \frac{1}{2}\rho(h)V^2S\left(C_{D_0} + KC_L^2\right) \tag{103}$$

$$C_L \approx \frac{2\left(mV\dot{\gamma} + W\right)}{\rho(h)V^2S} \tag{104}$$

Thus, the lift coefficient can be computed directly as a function of $\gamma(t)$, $V(t)$, and h. Typically, the lift coefficient attains a maximum value of almost 1 when the wing is stalled without flap deployment. So, $\gamma(t)$ and $V(t)$ should be specified such that the lift coefficient does not exceed the maximum lift coefficient. Typically, the cruise lift coefficient should be set to be no greater than 0.7 and the landing lift coefficient should be set to be no greater than 1.3. The lift coefficient is then used to determine the lift circulation strength for the wake vortex interaction model.

2. *Turning Flight*

If the aircraft motion is restricted to a turning flight in a horizontal plane, then $\gamma = 0$, $\dot{V} = 0$, $\dot{h} = 0$, and

$$\dot{x} = V\cos\psi \tag{105}$$

$$\dot{y} = V\sin\psi \tag{106}$$

$$\dot{\gamma} = \frac{T\sin\alpha + L\cos\phi - W}{mV} \tag{107}$$

$$\dot{\psi} = \frac{L\sin\phi}{mV} \tag{108}$$

Since $\gamma = 0$, $\dot{\gamma} = 0$ and $\alpha \approx 0$, we have

$$L\cos\phi \approx W \tag{109}$$

$$\dot{\psi} \approx \frac{W\tan\phi}{mV} \tag{110}$$

If a turning trajectory is prescribed by $\psi(t)$, then $\dot{\psi}(t)$ can be computed. The bank angle ϕ and the lift coefficient are then determined as

$$\phi = \tan^{-1}\frac{mV\dot{\psi}}{W} \tag{111}$$

$$C_L = \frac{2W}{\rho(h)V^2 S\cos\phi} \tag{112}$$

The load factor n is defined as

$$n = \frac{L}{W} = \frac{1}{\cos\phi} \tag{113}$$

Typically aircraft is designed to meet a load factor limit of about 2 to 2.5. So, $\psi(t)$ should be specified such that the load factor does not exceed the limit. Also, since the lift force increases during a turn, the drag force also increases according to

$$D = \frac{1}{2}\rho(h)V^2 S C_{D_0} + \frac{2W^2}{\rho(h)V^2 S\cos^2\phi} \tag{114}$$

For the airspeed to remain constant, i.e., $\dot{V} = 0$, the engine thrust must also increase to match the drag increase. There is also a maximum thrust limit. So, $\psi(t)$ should be specified such that the drag increase does not exceed the maximum engine thrust limit. The computed lift coefficient allows the wake-induced downwash to be computed during a turning flight.

III. Simulations

Two different simulations are performed to illustrate the wake vortex interaction for UAM.

A. Two Aircraft Simulation

In the first simulation, two UAM aircraft, a fixed-wing and a rotorcraft, are flying ahead of an aircraft that is scheduled to arrive at a specified location. We are interested in providing the wake-induced velocity field at this incoming aircraft location. The fixed-wing aircraft has a wing span of 30 ft and weighs 5,000 lbs. The fixed-wing aircraft CG is initially at $(0,0,-1000)$ ft. The rotorcraft weighs 1,500 lbs with a rotor diameter of 15 ft. The rotorcraft CG is initially at $(0,50,-1000)$ ft. The fixed-wing aircraft and rotorcraft are flying in a straight and level course at constant zero heading angles (due north) at constant airspeeds of 200 ft/sec and 150 ft/sec, respectively. The wake turbulence velocity at an incoming aircraft location $(-50,16,-1000)$ ft downstream of these aircraft is to be computed.

The lift circulation strength of the fixed-wing aircraft is computed as

$$\Gamma_0 = \frac{2W}{\pi\rho V b} \tag{115}$$

where W is the aircraft weight, ρ is the air density, $V = \sqrt{u^2+v^2+w^2}$ is the airspeed, and b is the wing span. The rotorcraft is equipped with an articulated rotor capable of providing flapping motion and cyclic pitch control. Therefore, the lift circulation strength of the rotorcraft is computed by Eq. (76)

$$\Gamma_0 = \frac{3W}{N\rho R^2\Omega} \tag{116}$$

where N is the number of rotor blades, R is the rotor radius, and Ω is the rotor speed which is equal to 1200 rpm. The corresponding blade flapping and cyclic pitch control are computed and plotted in Figure 13. The following parameters are obtained: $\theta_0 = 6.27^\circ$, $\theta_{1s} = -27.24^\circ$, $\theta_{1c} = 0^\circ$, $\beta_0 = 2.90^\circ$, $\beta_{1s} = -0.61^\circ$, and $\beta_{1c} = 25.49^\circ$. The contour plots of the normalized lift circulation $\Gamma_n = \frac{\Gamma}{R\Omega c}$ and lift $L_n = \frac{L}{\frac{1}{2}\rho R^2\Omega^2 c}$ are shown in Figures 14 (a) and (b), respectively. The local lift circulation is seen to be larger on the retreating side than it is on the advancing side, but the lift distribution is radially more uniform except for the region near the rotor tip.

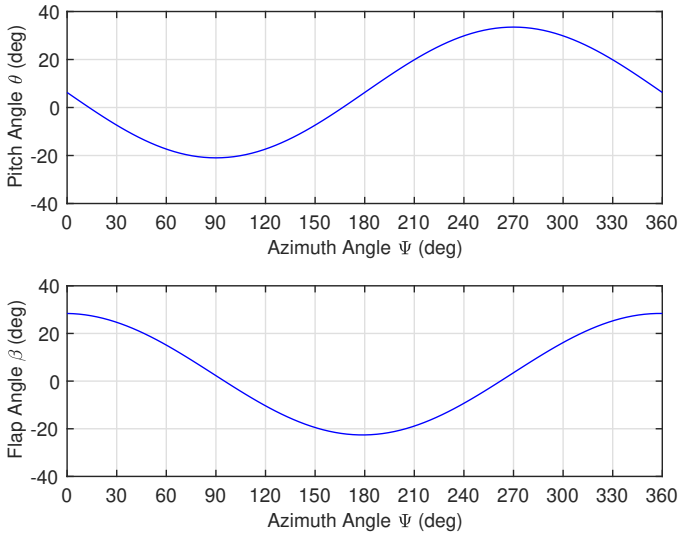

Figure 13. Rotorcraft Blade Flapping and Cyclic Pitch Control

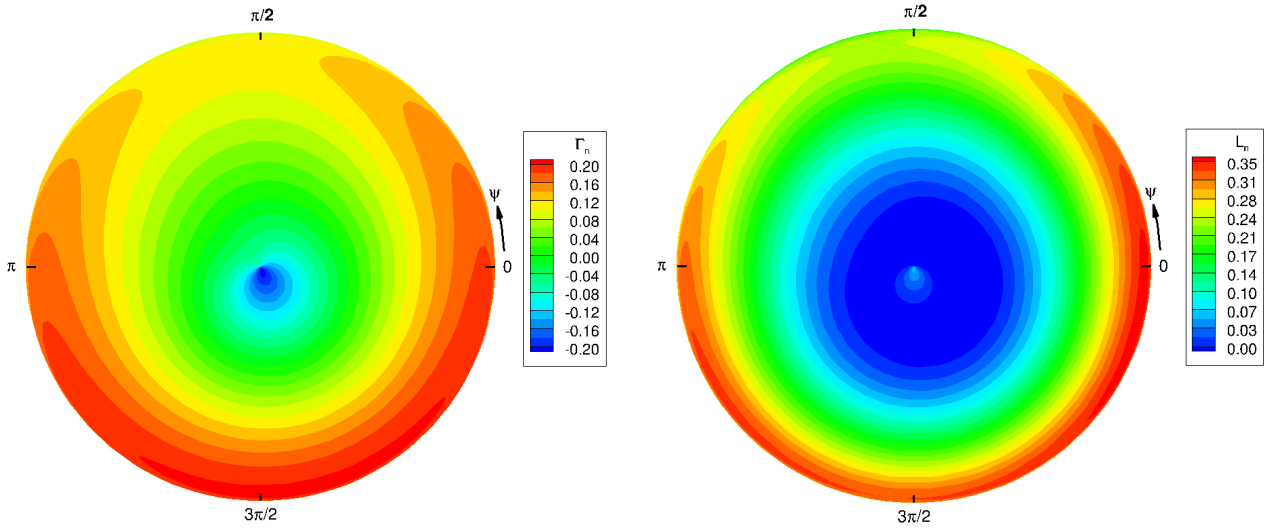

(a) (b)

Figure 14. Normalized Lift Circulation and Lift

The wake interaction of the fixed-wing aircraft and rotorcraft at the initial time is plotted in Fig. 15.

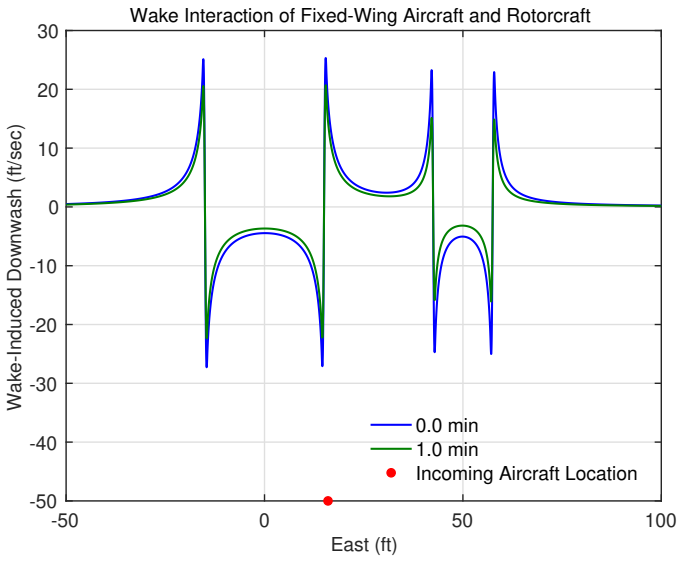

Figure 15. Wake Vortex Interaction Due to Two Aircraft

For the wake propagation model, the wake propagation parameter for the fixed-wing aircraft is estimated to be $\beta = 3.3501 \times 10^{-5}$ and the wake propagation parameter for the rotorcraft is estimated to be $\beta = 6.7002 \times 10^{-5}$ corresponding to 1% reduction in the initial lift circulation strength for a 10 wing span distance. The downstream distance of the incoming aircraft from the fixed-wing aircraft and rotorcraft is 50 ft. At this distance, the wake propagation model predicts a lift circulation strength of 99.83% of the initial lift circulation strength of the fixed-wing aircraft and a lift circulation strength of 99.67% of the initial lift circulation strength of the rotorcraft.

For the wake age model, an eddy dissipation parameter is chosen to be $\varepsilon^* = 0.03$ for low turbulence. This corresponds to a wake age parameter $\alpha = 0.04887$. The wake decay at the incoming aircraft location is shown in Figure 16. As can be seen, the wake decay is faster for the rotorcraft than for the fixed-wing aircraft.

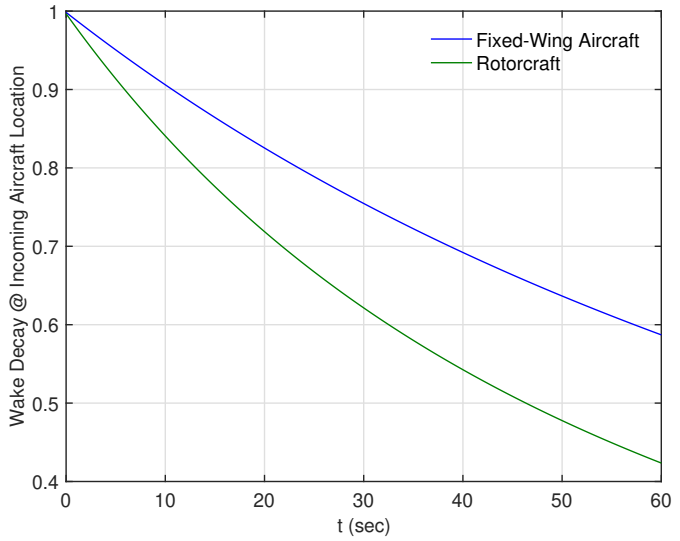

Figure 16. Wake Decay Effect

Due to the simplifying assumption that all the aircraft are flying at the same altitude and constant zero heading angles, the wake-induced velocity only has a non-zero vertical component. The wake-induced downwashes at the

incoming aircraft location due to the fixed-wing aircraft and rotorcraft are presented in Figures 17 and 18. The negative value indicates an upwash. It can be seen that the wake-induced downwash at the incoming aircraft location is predominantly contributed by the wake vortex generated by the right wing of the fixed-wing aircraft.

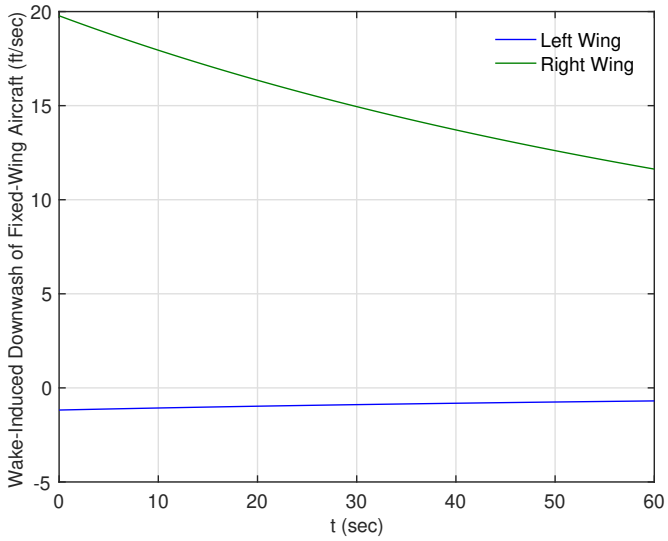

Figure 17. Wake-Induced Downwash @ Incoming Aircraft Location due to Fixed-Wing Aircraft

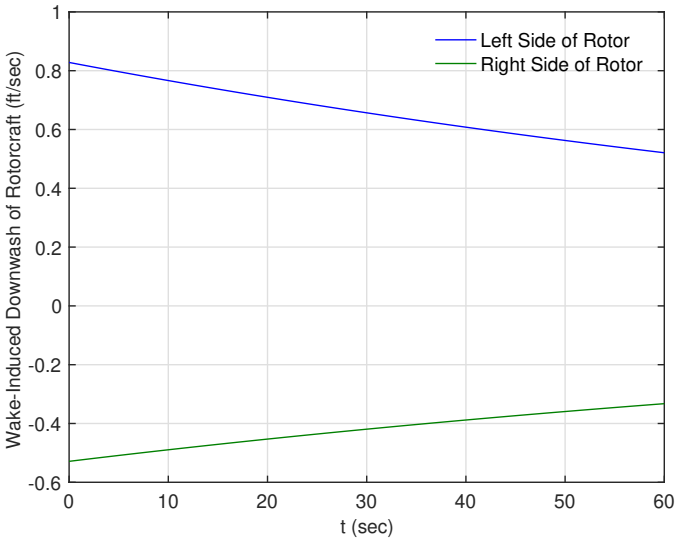

Figure 18. Wake-Induced Downwash @ Incoming Aircraft Location due to Rotorcraft

The total wake-induced downwash at the incoming aircraft location is computed by summing all the individual wake-induced downwash contributions of the fixed-wing aircraft and rotorcraft. This is shown in Fig. 19. As can be seen, the initial wake-induced downwash is 18.90 ft/sec. After 60 sec, the downwash decays to 11.06 ft/sec.

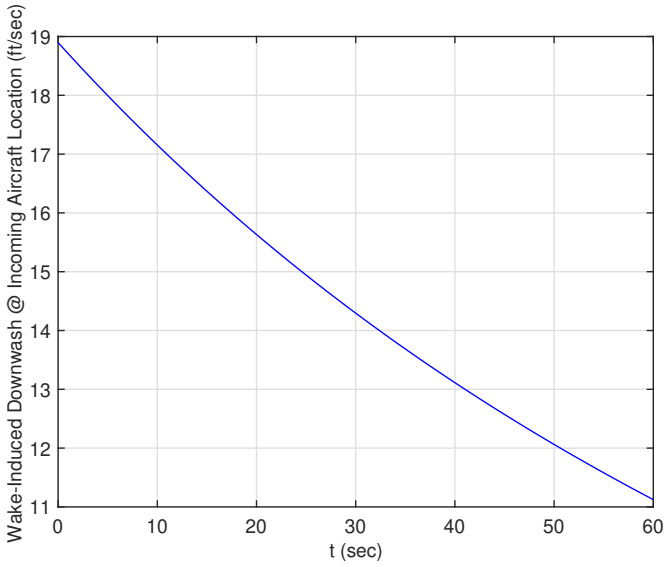

Figure 19. Wake-Induced Downwash @ Incoming Aircraft Location due to Fixed-Wing Aircraft

B. Multi-Aircraft Simulation

A four aircraft simulation is performed to illustrate a typical UAM operation in a high-density scenario. The four aircraft are two fixed-wing aircraft each weighing 5,000 lbs with a wing span of 30 ft flying at 200 ft/sec, and two rotorcraft each weighing 1,000 lbs with a rotor diameter of 15 ft flying at 150 ft/sec. Fixed-wing aircraft 1 is initially at $(126, 0, -1000)$ ft flying at constant zero heading angle, fixed-wing aircraft is initially at $(123, -31, -1000)$ ft flying at a constant heading angle of -10°, rotorcraft 3 is initially at $(70, 56, -1000)$ ft flying at a constant heading angle of 25°, and rotorcraft 4 is initially at $(-50, 132, -1000)$ ft flying at a constant heading angle of 90°. Figure 20 shows the flight paths of the aircraft which all intersect at the incoming aircraft location.

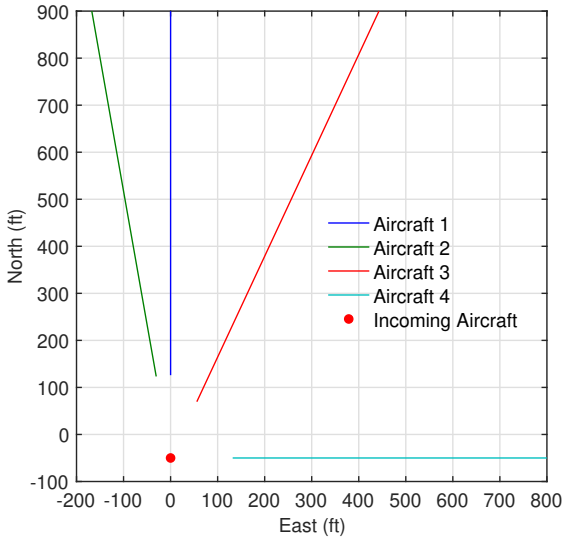

Figure 20. Flight Paths of Four Aircraft

Figure 21 shows the contour plot of the wake vortex interaction in the airspace region that centers at the incoming

aircraft coordinate $(-50, 0, -1000)$ ft at 4 sec. As can be seen, the wake vortex interaction creates a complex wake-induced velocity field. The wing tip vortices created from the four aircraft can be seen in the contour plot.

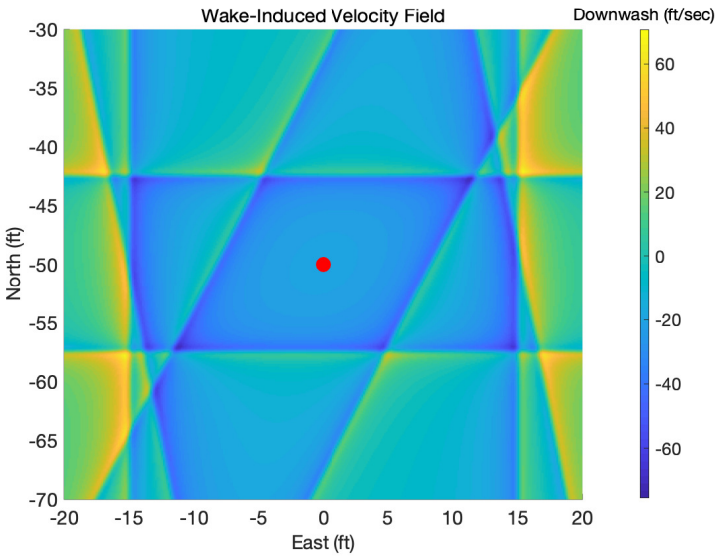

Figure 21. Wake-Induced Velocity Field Due to Four-Aircraft Wake Vortex Interaction

Figure 22 shows the wake-induced downwash decay at the incoming location. After 60 sec, the downwash decreases from the initial value of 21.35 ft/sec to 10.67 ft/sec.

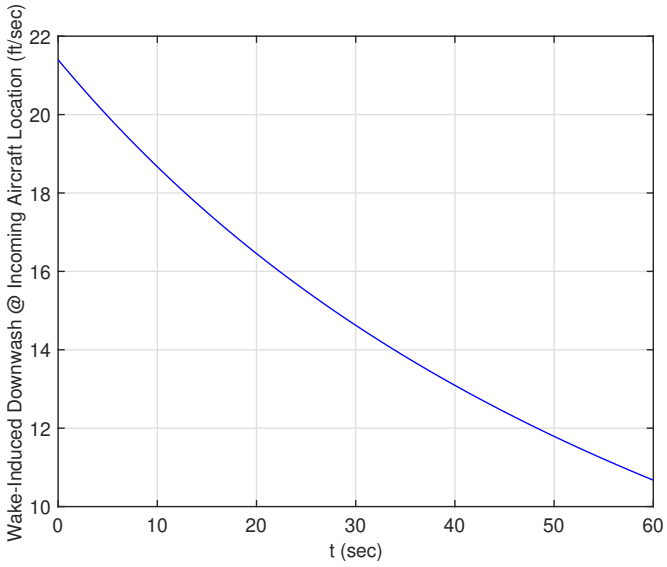

Figure 22. Wake Decay at Incoming Aircraft Location Due to Four-Aircraft Wake Vortex Interaction

IV. Conclusion

In this study, we develop an improved wake vortex interaction modeling approach for urban air mobility vehicles. A simplified wake age model is developed that accounts for both the temporal and spatial dissipation of the lift circulation strength. This simplified model is based on a three-phase wake decay model developed by Proctor et

al. An improved wake vortex model for rotorcraft is developed to account for the unsteady lift developed by the blade flapping motion and cyclic pitch control. The model removes the lift asymmetry observed in a previous study as a result of the blade flapping and cyclic pitch control. A wake interaction modeling approach is presented that accounts for the aircraft motion in steady and maneuvering flight. Multi-aircraft simulations are performed to illustrate a wake vortex interaction scenario that may exist in a high-density UAM operation.

Future work will explore the wake vortex interaction with buildings and vertiports. The safety consideration of rotorcraft operating in near wake may also be an important subject to investigate for UAM operation. Multi-rotor UAM wake vortex modeling is also an area of interest to be considered.

Acknowledgment

This work was supported by the System-Wide Safety (SWS) project under the Airspace Operations and Safety Program within the NASA Aeronautics Research Mission Directorate (ARMD).

References

[1]Ellis, K., Koelling, J., Davies, M., and Krois, P., "In-time System-wide Safety Assurance (ISSA) Concept of Operations and Design Considerations for Urban Air Mobility (UAM)," NASA/TM-2020-5003981, 2020.

[2]Young, S., Ancel, E., Moore, A., Dill, E., Quach, C., Foster, J., Darafsheh, K., Smalling, K., Vazquez, S., Evans, E., et al., "Architecture and Information Requirements to Assess and Predict Flight Safety Risks During Highly Autonomous Urban Flight Operations," NASA Report, 2020.

[3]Brashears, M.R. and Hallock, J.N., "Aircraft Wake Vortex Transport Model," AIAA Journal of Aircraft}, Vol. 11}, No. 5, p. 265-272, 1974.

[4]Estevez, N., "Consolidated Wake Turbulence (CWT) Separation Standards," U.S. Department of Transportation, Federal Aviation Administration, 2019.

[5]Nguyen, N., "A Physics-Based Spatial Wake Interactional Model of Fixed-Wing Aircraft and Rotorcraft for Urban Air Mobility," AIAA Intelligent Systems Conference, AIAA-2021-0881, January 2021.

[6]Proctor, F.H., Ahmad, N.N., Switzer, G.S., Duparcmeur, F.M.L., "Three-Phased Wake Vortex Decay," AIAA Atmospheric and Space Environments Conference, August 2010.

[7]Katz, J., Plotkin, A., *Low-Speed Aerodynamics: From Wing Theory to Panel Methods*, MacGraw-Hill, 1991, p. 70, 137.

[8]Lamb, H., *Hydrodynamics*, 6^{th} Edition, Dover Publications, 1932, p. 592.

[9]Saffman, P. G., *Vortex Dynamics*, Cambridge University Press, 1992.

[10]Van Hoydonck, W. R. M., Haverdings, H., Pavel, M. D., "A Review of Rotorcraft Wake Modeling Methods for Flight Dynamics Applications," 35th European Rotorcraft Forum, 2009.

[11]Proctor, F. H., "Interaction of Aircraft Wakes from Laterally Spaced Aircraft," 47th AIAA Aerospace Sciences Meeting, AIAA-2009-343, January 2009.

[12]Robinson, G. H., Larson, R. R., "A Flight Evaluation of Methods for Predicting Vortex Wake Effects on Trailing Aircraft," NASA TN D-6904, November 1972.

[13]Delisi, D. P., Greene, G. C., Robins, R. E., Vicroy, D. C., Wang, F. Y., "Aircraft Wake Vortex Core Size Measurements," AIAA 21st Applied Aerodynamics Conference, June 2003.

[14]Butler, K. M., "Estimation of Wake Vortex Advection and Decay Using Meteorological Sensors and Aircraft Data," Report ATC-201, Lincoln Laboratory, September 1993.

[15]Theodorsen, T., "General Theory of Aerodynamic Instability and the mechanism of Flutter", NACA Report No. 496, 1949.

[16]Crimi, P., "Theoretical Prediction of the Flow in the Wake of a Helicopter Rotor: Part 1 - Development of Theory and Results of Computations," U.S. Army Ballistic Research Laboratory Final Report , Contract No. DA 30-069-AMC-645(R), September 1965.

[17]Caprace, D.-G., Chatelain, P., Winckelmans, G., "Wakes of Rotorcraft in Advancing Flight: A Large-Eddy Simulation Study," Journal of Physics of Fluids, Vol. 32, No. 087107, 2020.